Boundary-Layer Meteorology (2021) 181:523–542
https://doi.org/10.1007/s10546-020-00595-w

RESEARCH ARTICLE

# A Lagrangian Cloud Model for the Study of Marine Fog

**David H. Richter**[1] · **Theodore MacMillan**[1] · **Charlotte Wainwright**[1]

Received: 18 June 2020 / Accepted: 25 November 2020 / Published online: 14 January 2021


**Abstract**
A large-eddy simulation model is coupled with a Lagrangian cloud model to study marine fog. In this model, aerosols and droplets are treated from a Lagrangian frame of reference, in contrast to the traditional bulk and bin microphysical models. Droplet growth via condensation is governed by Köhler theory and environmental conditions local to the droplet. Coupling to the vapour and temperature fields of the flow ensures mass, momentum, and energy conservation between the air and droplet phases. Based on the recent C-FOG field campaign, a simulation is performed which highlights the benefits and potential of this type of model. By initializing the simulation with the measured aerosol size distribution and making assumptions about the chemical composition of the multiple peaks, the simulations provide a clear explanation for the observed bimodal droplet distribution during C-FOG: high supersaturation levels cause condensational growth of nearly all coarse-mode aerosols (presumed to be composed of marine salt), as well as a large number of accumulation model aerosols (presumed to be of continental origin with a lower hygroscopicity). The largest peak in the resulting droplet distribution is created from coarse-mode aerosols with high hygroscopicity, while the secondary peak is only possible due to the limited impact of the largest peak on saturation levels inside the fog. Thus, for the simulated levels of supersaturation, it is the limited number of coarse-mode aerosols which is responsible for the emergence of a larger second peak.

**Keywords** Fog · Large-eddy simulation · Lagrangian cloud model

## 1 Introduction

Recently, significant advances have been made in the development of so-called Lagrangian cloud models (LCMs), where parcels of cloud droplets are tracked from a Lagrangian perspective and interact with their local environment as they are advected throughout the domain (Andrejczuk et al. 2008; Shima et al. 2009; Sölch and Kärcher 2010; Riechelmann et al. 2012; Hoffmann et al. 2015). This is in contrast to the more traditional Eulerian cloud modelling approaches, including both bulk and spectral-bin microphysical models (Khain et al. 2015), where cloud droplet properties are stored on the computational grid and Eulerian equations

✉ David H. Richter
David.Richter.26@nd.edu

[1] University of Notre Dame, 156 Fitzpatrick Hall, Notre Dame, IN 46556, USA

are solved for their evolution in time at each grid point. The LCM approach has several key advantages over the Eulerian representation (Grabowski et al. 2019; Morrison et al. 2020), and numerically represents cloud physics in a more natural framework since microphysical processes are ultimately the end result of discrete droplets moving and evolving throughout a turbulent atmosphere.

As such, the LCM approach can seamlessly account for changes in the droplet size distribution (DSD), since the droplet collections (often referred to as "superdroplets"; Shima et al. 2009) are treated individually. As long as there are a sufficient number of computational superdroplets to represent and sample the full DSD, and as long as sufficiently accurate subgrid and collision-coalescence models are employed, the LCM provides an ideal tool for investigating the evolution of DSDs in various atmospheric environments. This inherently includes the process of droplet activation, since the superdroplets can individually grow if local supersaturations exceed the critical value for any particular droplet. In contrast, bulk microphysical approaches (e.g., Morrison et al. 2005), used for their computational efficiency, must a priori assume a DSD within each hydrometeor category, and thus are typically unable to represent DSD features such as bimodality (Korolev 1994). In these schemes, droplet activation is not resolved and assumptions are made regarding cloud condensation nuclei (CCN) availability. Furthermore, spectral-bin approaches, which discretize the droplet spectrum into a specified number of classes (and thus can represent the evolution of DSDs), can suffer from numerical discretization errors which stem from their Eulerian representation. Recently, Morrison et al. (2018) demonstrated that numerical diffusion in spectral-bin models causes an artificial broadening of the DSD, which can be erroneously interpreted as a genuine physical effect. The Lagrangian discretization suffers from no such numerical diffusion. The LCM approach also offers detailed information on the time history of Lagrangian parcels, and can provide a view of the lifecycle, including droplet activation, diffusional growth, collision/coalescence, and sedimentation that is simply unavailable using Eulerian approaches. Moreover, the dynamic coupling between the superdroplets and surrounding flow naturally takes into account two-way exchanges of heat and moisture, thereby avoiding the need for artificially removing all supersaturation during each model timestep as done in bulk model implementations (see discussion in Thouron et al. 2012).

While the LCM approach is certainly not at a stage where it can be used in applications such as operational numerical weather prediction, it is a technique well suited for better understanding and constraining processes which continue to plague bulk models. Noh et al. (2018) for instance use an LCM to calculate certain bulk model coefficients in the context of shallow cumulus clouds. Shima et al. (2009), while introducing the superdroplet concept of having each Lagrangian droplet in the model represent a parcel of many droplets with the same properties, demonstrate that the LCM approach can be used to understand collision-coalescence in cloudy environments. Unterstrasser et al. (2017) likewise use the LCM framework as a testbed for multiple collision kernels and critically evaluate their algorithmic implementations. And while it has long been recognized that turbulence must play a role in accelerating DSD broadening to achieve realistic rain formation rates (Shaw 2003; Grabowski and Wang 2012), the LCM approach coupled to direct numerical simulation (DNS) or large-eddy simulation (LES) offers a means for better quantifying and modelling this process at coarser scales (Hoffmann et al. 2017), including the investigation of processes like the so-called "eddy hopping" mechanism (Grabowski and Abade 2017). Finally, the very recent work of Schwenkel and Maronga (2020) applies the LCM approach to fog, as is done in this study, and demonstrates the clear differences between using LCM and bulk models. In several specific respects, the LCM provides more realistic fog evolution owing to the more physically-based treatment of gravitational settling and CCN activation.

In this work, we combine the LCM approach with LES for representing marine fog conditions encountered during the recent C-FOG campaign (Fernando et al. 2020). In our companion study, Wainwright and Richter (2020) explore the sensitivities associated with representing marine fog using LES and the single-moment bulk microphysical scheme of Morrison et al. (2005)—a similar approach to other LES studies of fog (Nakanishi 2000; Maronga and Bosveld 2017). Changes in model variables, in particular the droplet number concentration assumed in the microphysical scheme, are found to cause significant changes to the resulting fog properties. Thus in the present work, we explore the feasibility of using the LCM approach for investigating marine fog, and highlight the practical and scientific advantages to using such a framework.

## 2 Model Set-up

### 2.1 Large Eddy Simulation Model

The model used is the National Center for Atmospheric Research Turbulence with Lagrangian Particle (NTLP) model (Sweet et al. 2018), whose foundation is the LES code of Moeng (1984), Sullivan et al. (1994), and Sullivan and Patton (2011). The LES component uses a low-storage, third-order Runge–Kutta (RK3) scheme (Spalart et al. 1991) to solve the filtered, incompressible Navier–Stokes equations under the Boussinesq approximation for mass, momentum, and energy conservation

$$\nabla \cdot \mathbf{u} = 0, \tag{1}$$

$$\frac{\partial \mathbf{u}}{\partial t} + \mathbf{u} \cdot \nabla \mathbf{u} = -\mathbf{f} \times \left(\mathbf{u} - \mathbf{U}_\mathrm{g}\right) - \nabla \pi + \hat{\mathbf{k}} \frac{g}{\theta_0} \theta_v - \nabla \cdot \mathbf{T} + \mathbf{S}_\mathrm{m}, \tag{2}$$

$$\frac{\partial \theta}{\partial t} + \mathbf{u} \cdot \nabla \theta = -\nabla \cdot \mathbf{\Theta} + \left(\frac{P}{P_0}\right)^{R_\mathrm{d}/c_\mathrm{p,a}} \left(S_\mathrm{T} + S_\mathrm{rad}\right), \tag{3}$$

$$\frac{\partial q_v}{\partial t} + \mathbf{u} \cdot \nabla q_v = -\nabla \cdot \mathbf{Q} + S_\mathrm{v}, \tag{4}$$

where $\mathbf{u}$ is the filtered velocity vector, $\theta$ is the filtered potential temperature, and $q_\mathrm{v}$ is the filtered water vapour mixing ratio, defined as $q_v = \rho_v / \rho_a$ where $\rho_v$ is the local (variable) water vapour density (or absolute humidity) and $\rho_a$ is the constant density of dry air. Furthermore, $\mathbf{f} = f\hat{\mathbf{k}}$ where $f = 1 \times 10^{-4}\ \mathrm{s}^{-1}$ is the Coriolis parameter and $\hat{\mathbf{k}}$ is the unit vector in the vertical ($z$) direction; $\mathbf{U}_\mathrm{g} = \left[U_\mathrm{g}, V_\mathrm{g}\right]$ is the applied geostrophic wind vector; $\pi$ is a pressure variable whose Poisson equation enforces incompressibility; $g$ is the acceleration due to gravity; $\theta_0 = 273$ K is a reference temperature; $P$ and $P_0$ are the hydrostatic pressure and a reference pressure, respectively, defined as $P = P_0 - \rho_a g z$ and $P_0 = 1013.25$ hPa; $R_\mathrm{d}$ and $c_\mathrm{p,a}$ are the gas constant and specific heat of dry air, respectively, and are defined in Table 1 below.

In Eqs. 1–4, the terms $\mathbf{T}$, $\mathbf{\Theta}$, and $\mathbf{Q}$ refer to the subgrid fluxes of momentum, potential temperature, and water vapour, respectively, and are calculated based on the model of Deardorff (1980), which solves an additional prognostic equation for subgrid energy $e$; for additional details see Moeng (1984) or Sullivan et al. (1994). The terms $S_\mathrm{T}$ and $S_\mathrm{v}$ refer to the sources of heat and water vapour due to the Lagrangian droplets. The mathematical expressions for these quantities are provided in a subsequent section, but they physically represent mass and energy exchange between the gas and liquid phases as the droplets change size and temperature due to their local environment. Likewise, the source $\mathbf{S}_\mathrm{m}$ represents momentum

conservation between the air and the droplets, and as such implicitly accounts for sinking tendencies owing to cloudy air. Finally, the source $S_{\text{rad}}$ in the heat equation (to be defined below) is the longwave radiative source due to the presence of the droplets.

## 2.2 Superdroplet Model

### 2.2.1 Evolution Equations

The NTLP model is equipped with individual droplet physics based on the microphysical formulations described in Pruppacher and Klett (1997) and elsewhere. Additional details of the NTLP numerical implementation can be found in Helgans and Richter (2016), but those pertaining specifically to the LCM model are provided here. The primary difference between the present study and previous uses of the NTLP model (Peng and Richter 2017, 2019; Sweet et al. 2018) is that the current work implements the superdroplet method of Shima et al. (2009), allowing the $i$th numerical particle (i.e., the superdroplet) to represent a cluster of droplets, with the superdroplet multiplicity $\xi^i$ indicating the number of droplets contained within. Thus the total number of aerosols/droplets in the entire computational domain is the sum $N_{\text{total}} = \sum_{i=1}^{N_\text{p}} \xi^i$, where $N_\text{p}$ is the number of superdroplets. In the limit of infinite computational power, the multiplicity would approach unity (i.e., every particle in the system would be represented individually), but the total number of superdroplets is roughly limited to $N_\text{p} \sim \mathcal{O}(10^6)$ for practical purposes in the present study.

Following the framework of Shima et al. (2009), the droplets represented by each superdroplet possess a common position $\mathbf{x}_\text{p}^i$, radius $r_\text{p}^i$, temperature $T_\text{p}^i$, velocity $\mathbf{v}_\text{p}^i$, solute mass $m_\text{s}^i$, and hygroscopicity $\kappa^i$. At each timestep, the NTLP code solves the Lagrangian equations governing momentum, mass, and energy conservation for each of the $i$th superdroplets:

$$\frac{d\mathbf{x}_\text{p}^i}{dt} = \mathbf{v}_\text{p}^i, \tag{5}$$

$$\frac{d\mathbf{v}_\text{p}^i}{\text{d}t} = \frac{1}{\tau_\text{p}}\left(\mathbf{u}_\text{f} - \mathbf{v}_\text{p}^i\right) - g\hat{\mathbf{k}}, \tag{6}$$

$$\frac{dr_\text{p}^i}{\text{d}t} = \frac{1}{9}\frac{Sh_p}{Sc}\frac{\rho_\text{p}}{\rho_\text{w}}\frac{r_\text{p}^i}{\tau_\text{p}}\left(q_\text{f} - q_*\right), \tag{7}$$

$$\frac{dT_\text{p}^i}{\text{d}t} = -\frac{1}{3}\frac{Nu_p}{Pr}\frac{c_{\text{p,a}}}{c_\text{L}}\frac{\rho_\text{p}}{\rho_\text{w}}\frac{1}{\tau_\text{p}}\left(T_\text{p}^i - T_\text{f}\right) + 3L_\text{v}\frac{1}{r_\text{p}^i c_\text{L}}\frac{dr_\text{p}^i}{dt}, \tag{8}$$

while the solute mass $m_\text{s}^i$ and hygroscopicity $\kappa^i$ of each superdroplet are assumed constant in the current study, and specified via initial conditions (to be described below). In Eqs. 5–8, the local air velocity $\mathbf{u}_\text{f}$, specific humidity $q_f$, and temperature $T_\text{f}$ are calculated at the superdroplet location via sixth-order Lagrange interpolation from the LES grid. The gravitational acceleration $g$ only acts in the vertical direction ($\hat{\mathbf{k}}$). The droplet Stokes time scale, $\tau_p = 2\rho_p r_\text{p}^{i^2}/(9\nu_a\rho_a)$, is a measure of droplet inertia and indicates the time in which a droplet can adjust to the local air velocity. In addition to these quantities, Eqs. 5–8 contain a number of material properties and nondimensional parameters which are defined in Table 1. In particular, Eqs. 7 and 8 include the Sherwood ($Sh_\text{p}$) and Nusselet ($Nu_\text{p}$) numbers, which account for ventilation effects in droplet vapour and mass transfer from the droplet surface, as well as the Schmidt ($Sc$) and Prandtl ($Pr$) numbers, which specify the vapour and temperature diffusivities. In this study, we apply a simple random subgrid fluctuation to the

**Table 1** Model parameters

| Symbol | Description | Value/expression |
|---|---|---|
| $\nu_a$ | Kinematic viscosity of air | $1.57 \times 10^{-5}$ m$^2$ s$^{-1}$ |
| $\rho_a$ | Density of dry air | 1.2 kg m$^{-3}$ |
| $\rho_w$ | Density of pure water | 1000 kg m$^{-3}$ |
| $\rho_p$ | Density of droplet (inc. solute) | Variable |
| $c_{p,a}$ | Sp. heat of air at const. press. | 1006 J (kg K)$^{-1}$ |
| $c_{p,v}$ | Sp. heat of water vapour at const. press. | 1952 J (kg K)$^{-1}$ |
| $c_L$ | Specific heat of liquid water | 4179 J (kg K)$^{-1}$ |
| $L_v$ | Latent heat of vapourization | $2.44 \times 10^6$J kg$^{-1}$ |
| $R_d$ | Gas constant of dry air | 287 J (kg K)$^{-1}$ |
| $R_u$ | Universal gas constant | 8.314 J (mol K)$^{-1}$ |
| $M_w$ | Molecular weight of water | 0.018 kg mol$^{-1}$ |
| $M_s$ | Molecular weight of solute | 0.0584 kg mol$^{-1}$ |
| $\sigma$ | Air–water surface tension | $7.28 \times 10^{-2}$ N m$^{-1}$ |
| $Sc$ | Dimensionless Schmidt number | 0.615 |
| $Pr$ | Dimensionless Prandtl number | 0.71 |
| $Sh_p$ | Dimensionless Sherwood number | $Sh_p = 2 + 0.6 {Re_p}^{1/2} Sc^{1/3}$ |
| $Nu_p$ | Dimensionless Nusselt number | $Nu_p = 2 + 0.6 {Re_p}^{1/2} Pr^{1/3}$ |
| $Re_p$ | Droplet Reynolds number | $Re_p = 2 r_p^i \lvert \mathbf{v}_p^i - \mathbf{u}_f \rvert / \nu_a$ |

particle position at each timestep that is based on the LES eddy diffusivity (Park et al. 2020), but we do not implement subgrid fluctuations on the interpolated thermodynamic quantities (e.g., temperature and water vapour) due to the high resolution of the LES field. The more sophisticated subgrid dispersion model of Weil et al. (2004) has also been implemented in the code, however tests have indicated that the inclusion of either subgrid model has a very small effect in the current configuration.

An important quantity in Eq. 7 is $q_*$, which represents the specific humidity at the droplet surface. As is well known in Köhler theory (Rogers and Yau 1996; Pruppacher and Klett 1997), droplet surface curvature and a dissolved solute modify the surface vapour pressure from what would be expected at a flat air–water interface. This is encapsulated in our formulation for $q_*$

$$q_* = \frac{M_w}{R_u T_p^i \rho_a} e_s \exp\left[ \frac{L_v M_w}{R_u} \left( \frac{1}{T_f} - \frac{1}{T_p^i} \right) + \frac{2 M_w \sigma}{R_u \rho_w r_p^i T_p^i} - \frac{I \Phi_s m_s^i \, (M_w / M_s)}{\rho_w 4\pi {r_p^i}^3 / 3} \right], \quad (9)$$

where $\sigma$ is the air–water surface tension, $I = 2$ is the number of disassociated ions, and $\Phi_s$ is an osmotic coefficient. Furthermore, $e_s$ is the saturation vapour pressure evaluated at $T_f$; we use a modified version of the Magnus relation given by Alduchov and Eskridge (1996).

The last term in Eq. 9 reflects the solute effect on the droplet surface vapour pressure, and the solute composition determines the parameters $I$, $\Phi_s$, and $M_s$. Recently, Petters and Kreidenweis (2007) developed a simpler, single-parameter hygroscopicity model (known as $\kappa$-Köhler theory) which combines the effects of these solute parameters into a single hygroscopicity parameter $\kappa$. We have adopted this single-parameter formulation in our model

by assigning to each superdroplet its own specific, constant hygroscopicity $\kappa^i$, but in the framework of Eq. 9. In practice, this means we choose $I$ and $M_s$ to be constant values associated with marine salt (recognizing that this choice is arbitrary), and choose $\Phi_s$ as a free parameter which sets a desired value of $\kappa^i$. There is a one-to-one correspondence between our parameter $\Phi_s$ and the formulation of $\kappa$ in Petters and Kreidenweis (2007) which makes this unambiguous. As emphasized by Jensen and Nugent (2017), this solute effect on the droplet diffusional growth can be significant, and its explicit treatment in the LCM framework is an advantage over more traditional microphysical models.

Overall, the solution to Eqs. 5–8 yields the time evolution of position, velocity, size, and temperature as the droplets are carried throughout the domain. An additional computational consideration, however, is that the time scales associated with droplet evolution are very fast compared to those related to the turbulent flow resolved by LES (Andreas 1990; Veron 2015). Thus if Eqs. 5–8 were integrated explicitly in time using the same RK3 scheme as the LES, the timestep would be consequently limited to $\Delta t \sim \mathcal{O}(10^{-4}\ \mathrm{s})$—clearly too severe a limitation for simulations meant to investigate fog evolution for up to 12 h. As a result, Eqs. 5–8 are solved implicitly in time, using a traditional backwards Euler integration scheme. This method requires solving a nonlinear, coupled system of equations for the superdroplet position, temperature, and radius at each timestep, and this is achieved through a combined application of Newton–Raphson and Levenberg–Marquart iterations. We note that in many cloud studies, an equation for droplet temperature is not solved explicitly (e.g., Vaillancourt et al. 2002) since it adjusts so rapidly, but here we retain it for completeness, particularly for situations when the droplet temperature is not necessarily equal to its surroundings.

### 2.2.2 Collision/Coalescence

Finally, the framework of Shima et al. (2009) outlines a probablistic algorithm for incorporating droplet collision/coalescence, which is done by modifying the droplet radius $r_\mathrm{p}^i$, solute mass $m_\mathrm{s}^i$, and multiplicity $\xi^i$ of both interacting superdroplets according to rules of mass conservation. Briefly, particles within a certain region (Shima et al. 2009 choose the Eulerian grid cell; we define a volume $V$ independent of the LES grid) are subjected to a probability of collision

$$P_{jk} = E\left(r_\mathrm{p}^j, r_\mathrm{p}^k\right)\pi\left(r_\mathrm{p}^j + r_\mathrm{p}^i\right)^2 |\mathbf{v}_\mathrm{p}^j - \mathbf{v}_\mathrm{p}^k| \frac{\Delta t}{V}, \tag{10}$$

where $j$ and $k$ refer to two different superdroplets, and $E\left(r_\mathrm{p}^j, r_\mathrm{p}^k\right)$ refers to a collision efficiency to be specified (e.g., Hall 1980). Note that by using the full velocity difference in Eq. 10, we include potential effects of turbulence in addition to differential settling.

While this collision/coalescence algorithm has been implemented into the NTLP model and validated against the analytical Golovin (1963) solution, for the current study we have chosen not to use it. The reason for this is that while updating the droplet radii and multiplicities is based on liquid water mass conservation, the interaction of superdroplets with differing hygroscopicities $\kappa^j$ and $\kappa^k$ results in a less straightforward rule for the hygroscopicities after collision. Additionally, we have conducted tests with uniform hygroscopicity with collision/coalescence active, and found that for the fog conditions investigated herein, droplet collisions play no discernable role in the evolution of the fog. Furthermore, the largest droplets in the system rarely exceed a radius of 20 $\mu m$, making droplet collisions unlikely. The LCM work of Schwenkel and Maronga (2020) makes the same approximation. For these reasons we choose to apply more realistic values of $\kappa^i$ at the expense of including droplet

collision/coalescence since its effect is much more pertinent to fog dynamics, as seen below. A point of ongoing research is including hygroscopicity into the collision algorithm, using for example the simple mixing rule noted in Petters and Kreidenweis (2007).

## 2.3 Coupling

### 2.3.1 Vapour and Thermal Coupling

The two-way coupling of momentum, energy, and water mass is enforced in the NTLP model. Any momentum, energy, or mass gained/lost by a superdroplet residing within an LES grid cell is accounted for in the Eulerian fields of air velocity, potential temperature, and water vapour, respectively. The expressions for the source terms $\mathbf{S}_\mathrm{m}$, $S_\mathrm{T}$, and $S_\mathrm{v}$ are given below in terms of the droplet mass $m_\mathrm{p}^i = 4\pi\rho_\mathrm{p} {r_\mathrm{p}^i}^3/3$ and its rate of change $\dot{m}^i = \frac{dm_\mathrm{p}^i}{\mathrm{d}t} = 4\pi {r_\mathrm{p}^i}^2 \rho_w \frac{\mathrm{d}r_\mathrm{p}^i}{dt}$

$$\mathbf{S}_\mathrm{m} = -\sum_{\beta=1}^{N_\beta} \frac{w_\beta}{\Delta V} \xi^\beta \left( m_\mathrm{p}^\beta \frac{d\mathbf{v}_\mathrm{p}^\beta}{dt} + \dot{m}^\beta \mathbf{v}_\mathrm{p}^\beta \right), \tag{11}$$

$$S_\mathrm{T} = -\sum_{\beta=1}^{N_\beta} \frac{w_\beta}{\Delta V} \xi^\beta \left( -\frac{1}{3} \frac{Nu_p}{Pr} \frac{c_\mathrm{p,a}}{c_\mathrm{L}} \frac{\rho_\mathrm{p}}{\rho_\mathrm{w}} \frac{1}{\tau_\mathrm{p}} \left( T_\mathrm{p}^\beta - T_\mathrm{f} \right) + \dot{m}^\beta \left( c_\mathrm{p,v} T_\mathrm{f} - c_\mathrm{p,v} T_\mathrm{p}^\beta \right) \right) \tag{12}$$

$$S_\mathrm{v} = -\sum_{\beta=1}^{\mathcal{N}_\beta} \frac{w_\beta}{\Delta V} \xi^\beta \left( \frac{\dot{m}^\beta}{\rho_\mathrm{a}} \right). \tag{13}$$

In Eqs. 11–13, the summations are over all superdroplets $N_\beta$ which reside in the LES grid cell of volume $\Delta V$. The factor $w^\beta$ is a linear weight according to the proximity of the superdroplet to the nearest grid point. Thus each LES grid cell sums over all contributions from the droplets contained within each nearby superdroplet.

### 2.3.2 Radiation

In addition to the direct coupling terms, the presence of fog and clouds also influences the air properties via $S_\mathrm{rad}$—the net longwave radiative source due to the droplets. Following previous work on stratocumulus clouds which clearly shows the importance of longwave radiation effects on cloud-top entrainment and mixing (de Lozar and Mellado 2015; Mellado 2017), we implement a similar longwave parametrization to that of Mellado et al. (2018) which uses the simplified formulation developed by Larson et al. (2007). The longwave model is column-based, and uses the horizontally-averaged cloud properties. It is based on the upward-looking liquid water path

$$LWP(z) = \int_\mathrm{z}^{z_\infty} \rho_a \langle q_\mathrm{l} \rangle \, dz', \tag{14}$$

where $q_l$ is the total liquid water mixing ratio as a function of height, and the angle brackets refer to a horizontal average over the LES domain. The upper limit of the integral, $z_\infty$, is effectively the top of the domain. From the liquid water path, the formulation of Larson et al. (2007) yields the resulting radiation source

$$S_\mathrm{rad} = \frac{d}{\mathrm{d}z} \left[ F_\mathrm{r,ct} \mathrm{e}^{-\kappa_\mathrm{rad} LWP(z)} + F_\mathrm{r,cb} \mathrm{e}^{-\kappa_\mathrm{rad} (LWP(0) - LWP(z))} \right]. \tag{15}$$

In Eq. 15, $F_{\mathrm{r,ct}}$ and $F_{\mathrm{r,cb}}$ refer to prescribed constants that physically represent the net upward longwave radiative flux at the cloud top and cloud base, respectively. The constant $\kappa_{\mathrm{rad}}$ represents absorptivity. In the current study, which focuses on fog developing at the surface, we set $F_{\mathrm{r,cb}} = 0$. Guided by the values found by Larson et al. (2007) for their stratocumulus case, we set $F_{\mathrm{r,ct}} = 60\ \mathrm{W\,m^{-2}}$ and $\kappa_{\mathrm{rad}} = 120\ \mathrm{m^2\,kg^{-1}}$. An alternative approach to treating longwave radiation would be to instead account for it in the droplet temperature equation (Eq. 8), however this would require the extra complexities associated with describing radiative heat transfer on a per-droplet basis. We instead choose to retain a formulation as used in most Eulerian bin and bulk models.

## 2.4 Numerical Set-up

### 2.4.1 LES Set-up

The LES domain is similar to that of Wainwright and Richter (2020). The horizontal extent in the streamwise $x$ and spanwise $y$ directions are $L_x = 128$ m and $L_y = 128$ m, respectively. The vertical extent of the domain is $L_z = 128$ m, which is smaller than in typical boundary-layer LES studies but appropriate for the shallow advection fog layer which develops under the stable conditions described below. The grid spacing in the horizontal directions is $[\Delta x, \Delta y] = [1\ \mathrm{m}, 1\ \mathrm{m}]$, resulting in a grid size of $\left[N_x, N_y\right] = [128, 128]$. In the vertical direction, $N_z = 128$ grid points are stretched in the vertical, ranging between $\Delta z = 0.1$ m at the lower surface to $\Delta z = 6$ m at the domain top.

As in Wainwright and Richter (2020) we configure the simulation to represent advection fog, where a parcel of saturated, warm air suddenly encounters a lower sea-surface temperature (SST). This is accomplished by letting the turbulence spin up for 1 h while in thermal equilibrium with water surface, and then dropping the SST by 2 K, thereby mimicking the process of a saturated air mass in equilibrium with the lower surface abruptly being transported over cooler waters. Initially the SST is set to 284 K, and at 1 h is dropped to 282 K. The flow is forced with a constant geostrophic wind velocity with components $U_{\mathrm{g}} = 4\ \mathrm{m\,s^{-1}}$ and $V_{\mathrm{g}} = 0$. An initial thermodynamic profile is constructed based qualitatively on conditions encountered on the C-FOG campaign—i.e., slightly stable stratification at near saturation capped with a shallow inversion layer—and is presented in Fig. 1a.

For the LES, the boundary conditions are as follows. Periodicity is enforced in the $x$ and $y$ directions. At the upper boundary ($z = L_z$), a no-flux condition is applied for momentum, energy, and water vapour. At the lower surface, Monin–Obukhov similarity theory is employed to calculate surface fluxes with a roughness length of $z_0 = 3.2 \times 10^{-5}$ m. A uniform SST is used as described above, and $q_{\mathrm{v}}$ is fixed based on the SST such that the surface is always at 100% saturation.

### 2.4.2 Droplets and Aerosols

For the fog droplets and aerosols, superdroplets are distributed randomly throughout the entire domain at $t = 0$. Since the initial humidity field is below saturation throughout the entire domain, the initial superdroplets begin unactivated, and only activate as local supersaturation fluctuations exceed their critical value as the simulation evolves. In order to specify their initial size, composition, and solute mass, we use data from a fog event encountered during the C-FOG cruise, which characterizes the dry aerosol size distribution (see the green line in Fig. 1b). As is commonly observed, the distribution of dry aerosol diameter $d_{\mathrm{a}}$ is bimodal,

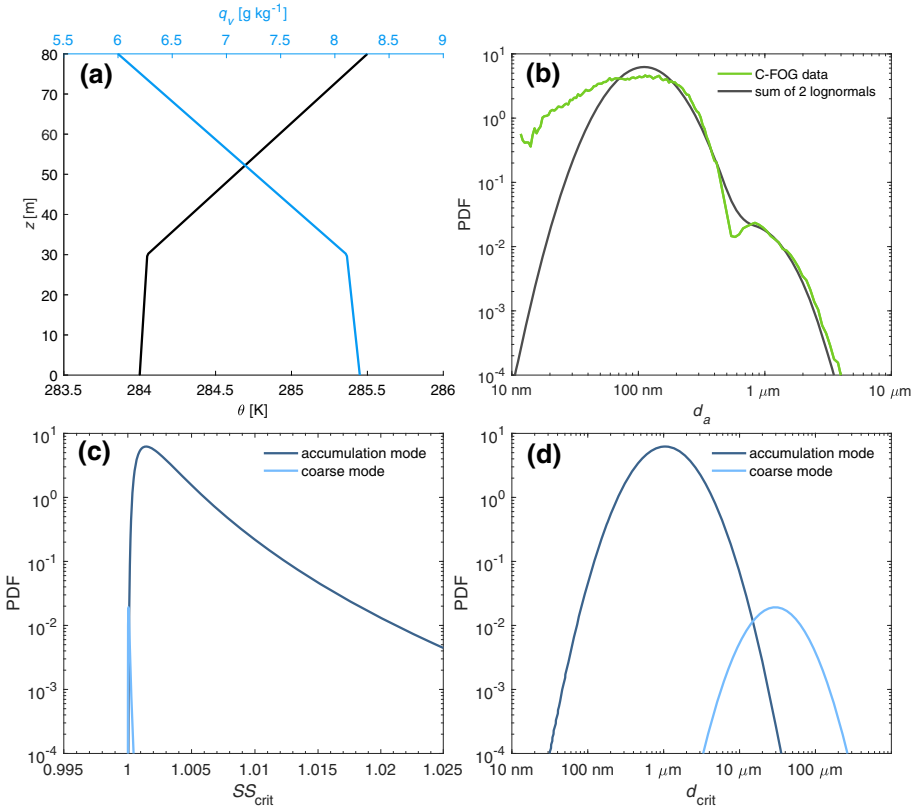


**Fig. 1** **a** The initial profiles of potential temperature $\theta$ (black) and water vapour mixing ratio $q_v$ (blue); **b** The initial probability density function (PDF) of the dry aerosol diameter $d_a$ as calculated by Eq. 16 (black) compared to data collected during the C-FOG campaign (green); **c** PDF of critical supersaturation values for the dry aerosol spectrum shown in **b**; **d** PDF of the critical diameter corresponding to **b** and **c**

with peaks centred roughly at $d_a \approx 0.1$ μm and $d_a \approx 1$ μm. We interpret these as the peaks of the accumulation and coarse aerosol modes, respectively, and accordingly model this dry aerosol size distribution $P_{a,init}$ as the sum of two lognormal probability density functions (PDFs)

$$P_{a,init}(d_a) = \frac{1}{1+\gamma}\frac{1}{S_a d_a \sqrt{2\pi}}\exp\left(\frac{-(\ln(d_a)-M_a)^2}{2S_a^2}\right) + \frac{\gamma}{1+\gamma}\frac{1}{S_c d_a \sqrt{2\pi}}\exp\left(\frac{-(\ln(d_a)-M_c)^2}{2S_c^2}\right). \quad (16)$$

The parameters $M_a = -1.95$, $S_a = 0.5$, $M_c = 0$, and $S_c = 0.45$ specify the location and width of the accumulation and coarse-mode peaks, respectively, and the parameter $\gamma = 0.02$ is a multiplicative factor which reduces the probability of coarse-mode aerosols relative to that of the accumulation mode. These parameters were chosen to match the initial LCM distribution with the conditions found during the C-FOG event.

At the initialization of the simulation, each of the $N_\mathrm{p}$ superdroplets draws a dry aerosol size $d_\mathrm{a}$ from the distribution $P_{\mathrm{a,init}}$. In practice, this is done by using the factor $\gamma$ to probabilistically determine whether the superdroplet will be from the accumulation or coarse-mode regime, and then once this is decided, the dry diameter $d_\mathrm{a}$ is drawn from the lognormal distribution associated with that mode. This is done by comparing a uniformly distributed random number with the cumulative distribution of the respective lognormal distribution. As these are the dry diameters, this effectively determines the solute mass $m_\mathrm{s}^i$ of this superdroplet, assuming a solute density of $\rho_\mathrm{s} = 2000$ kg m$^{-3}$. With $m_\mathrm{s}^i$, Eq. 9 is then used to hydrate this aerosol to the ambient humidity of the initial condition. This final size provides the initial condition on $r_\mathrm{p}^i$ for each of the $N_\mathrm{p}$ superdroplets. The initial superdroplet temperature $T_\mathrm{p}^i$ is set to the ambient temperature.

A significant advantage of using the LCM approach for the fog microphysics is that each superdroplet possesses its own solute mass—in this case chosen from a specified distribution. In addition, we can also assign each superdroplet its own hygroscopicity $\kappa^i$ as well. Over the ocean, with the exception of extremely remote areas, the accumulation mode is often anthropogenic in origin, while the coarse-mode is often composed primarily of marine salt (Zhang et al. 2014). For the present simulations, this dichotomy is captured in a simple way by setting all hygroscopicities from the accumulation mode to $\kappa^i = 0.6$, and all hygroscopicities from the coarse-mode to $\kappa^i = 1.2$, reflecting rough estimates of continental and marine values, respectively (Petters and Kreidenweis 2007). In Fig. 1c, d, the PDFs of the critical supersaturation and critical diameter, respectively, are shown for both the coarse and accumulation mode distributions. Due to the larger hygroscopicity, the coarse-mode aerosols have a much lower critical supersaturation, as well as critical diameters which can approach tens or even hundreds of micron in size.

Finally, based on data collected during the C-FOG campaign, we assign an initial bulk number concentration $N_\mathrm{c} = 800$ cm$^{-3}$ for the total number of accumulation and coarse-mode aerosols in the domain. For a particular choice of $N_\mathrm{p}$ (discussed below), this sets the multiplicity $\xi^i$ for each superdroplet.

From the Lagrangian perspective, the superdroplet number $N_\mathrm{p}$ plays the same role as grid resolution in the Eulerian solver: in the limit of very high $N_\mathrm{p}$, the aerosol solution is "exact" in the sense that every aerosol in the domain would be resolved. In practice, however, computational resources limit this number. According to Shima et al. (2009), a choice $N_\mathrm{p}$ should provide $\mathcal{O}(100)$ superdroplets in each of the Eulerian grid cells, since this would be adequate for representing the full DSD at each of the LES grid nodes. In the present work, this would require $N_\mathrm{p} = \mathcal{O}(10^8)$ superdroplets. Owing to the very high spatial resolution of the LES grid, as well as the large computational expense of this many superdroplets, we choose $N_\mathrm{p} = 10^6$, with ongoing work to both quantify the sensitivity of the results to $N_\mathrm{p}$ as well as boost computational efficiency [e.g., our efforts on porting the superdroplet calculation to graphical processing units (GPUs) are introduced in Sweet et al. 2018]. By comparison, the LCM fog study of Schwenkel and Maronga (2020) uses a much larger value of $N_\mathrm{p} = 7 \times 10^8$ on a somewhat coarser grid. In the present study, the multiplicity of the coarse and accumulation mode aerosols are chosen to be different, since there is an abundance of accumulation mode particles relative to coarse-mode particles and it was deemed inefficient to assign the $N_\mathrm{p}$ superdroplets evenly across the entire DSD. The multiplicity of coarse-mode superdroplets is 200 times lower than those of the accumulation mode, and as a result the coarse-mode peak is better resolved. A consequence of this, however, is that the bulk number concentration increases in time since coarse-mode aerosols are more prone to sedimentation; over the course of the simulations presented below, the bulk number concentration increases

by roughly a factor of two, but the vast majority of these extra aerosols are unactivated accumulation mode aerosols (discussed below).

Regarding boundary conditions for the droplets/aerosols. A no-flux condition is imposed at the upper boundary. At the bottom of the domain, droplets that hit the water surface are removed from the simulation, and a new superdroplet is immediately introduced randomly in the domain according to the same procedure for initialization. This maintains a constant number of superdroplets in the simulation throughout the entire duration so that certain statistics are quasi-steady-state.

### 2.4.3 Timestep of the Simulation

Finally, one last note must be included regarding the simulation timestep $\Delta t$. The Eulerian solver is limited by the Courant–Friedrichs–Lewy (CFL) condition since the advection term is solved explicitly. As noted above, the droplet evolution equations, which would normally be restricted to the small thermodynamic time scales of the droplet (related to $\tau_\mathrm{p}$), are solved implicitly so that larger timesteps can be employed. There is one final restriction, however, which results from the coupling terms $\mathbf{S}_\mathrm{m}$, $S_\mathrm{T}$, and $S_\mathrm{v}$, and is related to the so-called cloud or phase relaxation time scale $\tau_c \propto \tilde{N}_\mathrm{c}^{-1}\bar{r}_\mathrm{p}^{-1}$ (Squires 1952), where $\tilde{N}_\mathrm{c}$ is the local number concentration and $\bar{r}_\mathrm{p}$ the local mean radius within an LES grid cell. Physically, $\tau_c$ represents the rate at which the local droplet population can respond to changes in supersaturation. Numerically, the timestep must then be limited by $\tau_c$ since a larger $\Delta t$ could result in more moisture being removed than is available at certain locations within the flow. This is a problem which was analyzed in detail by Árnason and Brown (1971), and is generally true for any explicit time-stepping scheme. Thus for the present simulations the timestep is chosen as the minimum between that determined by the CFL condition and $\tau_\mathrm{c}/15$.

## 3 Results

Since the overall purpose of this work is to describe the LES–LCM approach and its application to marine fog, the results below are primarily demonstrative, illustrating that the method indeed captures realistic features of marine fog, while also providing physical insight and explanation which may be impossible to retrieve with more traditional microphysical models.

Figure 2 provides an instantaneous shapshot of the combined LES–LCM model. The background fields show a slice of local supersaturation, while the dots represent superdroplets within a 1-m slab of the background slice. The size of the dots is exaggerated, but their size and shading are selected to highlight the differences in droplet size throughout the domain. In particular, it is clear that within the fog layer (below 30 m), droplets are significantly larger than those above. Moreover, within the fog itself, fluctuations of supersaturation (up to 0.4%) are qualitatively seen to yield a broad size range; large droplets are seen to exist in regions of high supersaturation, while regions of zero or negative supersaturation correspondingly contain small droplets. Figure 2 thus provides visual evidence suggesting the process of stochastic condensation (Cooper 1989; Sardina et al. 2015; Chandrakar et al. 2016), where DSD broadening occurs in the absence of collision-coalesence due to random turbulent fluctuations in local supersaturation. This DSD broadening is shown in Fig. 4 below.

To characterize the overall development of the fog in the set-up described above, Fig. 3 displays multiple horizontally-averaged quantities of the fog as it develops over time and height. The SST is decreased at $t = 1$ h, and in this particular case the fog takes nearly 5

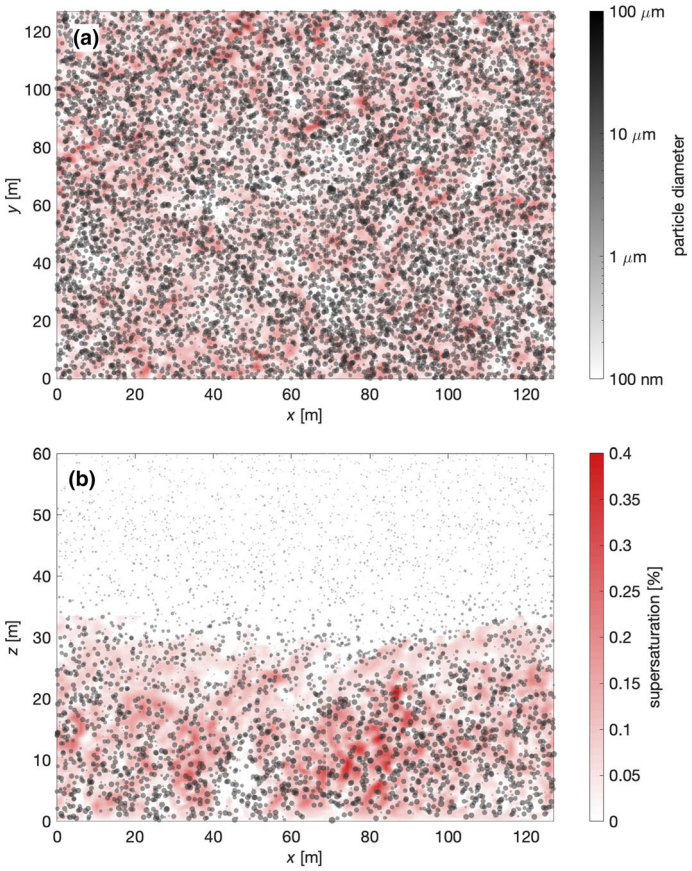


**Fig. 2** The background field of supersaturation (red) with the superdroplets overlaid (grey) for **a** a horizontal slice at $z = 20$ m and **b** a vertical slice from the centre of the domain at $y = 64$ m. All superdroplets within 1 m of each slice are shown, and their relative size is representative of the droplet diameter

h to develop after this point. Figure 3a shows the total liquid water mixing ratio $q_l$, which continues to thicken until the maximum time of the simulation. Defining the fog with a threshold of $q_l = 0.01$ g kg$^{-1}$ (as in Maronga and Bosveld 2017; Wainwright and Richter 2020), the white dashed lines outline its extent. As the fog develops, Fig. 3b shows that the total number concentration $N_c$ evolves from being spatially uniform at $t = 0$ to having regions of high and low concentration (note that $N_c$ includes all particles, regardless of size and activation state). In particular, after the onset of the fog, a layer of high $N_c$ develops near the fog top where the combination of elevated turbulence levels and dry air entrainment (and consequent droplet size reduction and/or deactivation) act to trap droplets in this location. We speculate that the settling of aerosols from the elevated, quiescent regions of the domain into the shear-generated turbulence at the fog top results in a build-up of number concentration as the effective sedimentation rate is diminished through the turbulence, and is not a numerical artifact.

Near the lower surface, the number concentration is lower, and Fig. 3c indicates that this is at least partially due to the relatively large mean droplet radius. Here, the mean droplet

radius exceeds 10 μm, but this rapidly diminishes with height throughout the entire duration of the fog. This is consistent with the idea that larger droplets settle more quickly than small ones, thereby increasing the average size while lowering the relative number concentration near the surface (Lewis and Schwartz 2004). Furthermore, the entrainment of relatively dry air from above into the fog layer leads to evaporation and thus generally smaller droplets near the top. Finally, Fig. 3d demonstrates one of the key features of the LCM: as the fog develops, a non-zero mean supersaturation can be maintained, which can approach 0.1%, with larger fluctuations as seen in Fig. 2. This value is almost certainly a function of the hygroscopic properties of the underlying aerosols as well as the background number concentration, and is slightly higher than typical values found in continental fog (for example Gerber 1991; Shen et al. 2018; Mazoyer et al. 2019). It is also a function of the superdroplet number $N_\mathrm{p}$ and its ratio to the number of grid points. As noted above, the ratio here is $\mathcal{O}(1)$, but would ideally be higher (Shima et al. 2009). With a higher ratio the supersaturation fluctuations would likely decrease, and this has been observed in test runs with $10x$ the value of $N_\mathrm{p}$ (which could only be run for a short duration due to computational expense), where the mean supersaturation reduced to roughly 0.06%. Furthermore, we note that other microphysical models, most notably some bulk schemes, remove all excess supersaturation at every timestep, though efforts have been made to investigate and alleviate this issue (e.g., Thouron et al. 2012; Boutle et al. 2018) and others have been modified to explicitly calculate supersaturation (Morrison and Grabowski 2008). The various quantities plotted in Fig. 3 also show evidence of large, infrequent, quasi-periodic, entrainment events, which result from coherent structures that occasionally form and dissipate. These are also seen in Wainwright and Richter (2020), and would require a larger domain extent to fully investigate.

For a more detailed look at the droplet evolution, Fig. 4 provides wire plots for the DSD as it advances in time (only droplets below $z = 30$ m are included in the DSD). From the initial distribution shown above in Fig. 1b, the fog onset at $t \approx 5$ h can be clearly seen by the emergence of a peak centred around $d_\mathrm{p} \approx 30$ μm. By the end of the simulation at $t = 9$ h, three distinct peaks are visible: the original peak of the accumulation mode which has shifted from $d_\mathrm{p} \approx 100$ nm to $d_\mathrm{p} \approx 170$ nm once they are hydrated, an intermediate peak at $d_\mathrm{p} \approx 3$ μm, and the rightmost peak at $d_\mathrm{p} \approx 30$ μm. Many similar qualitative features of the fog evolution are seen in the LCM model of Schwenkel and Maronga (2020), though for a different initial aerosol distribution.

In addition, the lower panel of Fig. 4 presents the evolution of the DSD measured during a marine fog event by an FM120 fog droplet monitor (Droplet Measurement Technologies, Longmont, Colorado, USA) onboard a research vessel during the C-FOG campaign. Notably, the observed DSD exhibits a clear bimodal signature, with a distinct trough located around $d_\mathrm{p} = 15 - 20$ μm, which persists throughout the entire fog event. This shape is well captured by the LES–LCM model, with the rightmost two peaks and trough located at nearly the same position as the measured data.

To better understand the overall shape of the numerically predicted DSD, as well as explaining the presence of dual peaks in the droplet size range (i.e., above $d_\mathrm{p} \approx 1$ μm) in both the numerical and observed data, the simulation data can be partitioned in multiple ways. First, the DSD at some time can be decomposed into the droplets that have activated versus those that have not, and these are presented in Fig. 5a, c. Evidence has been found of the presence of so-called giant CCN, which can hygroscopically grow to several microns in diameter without being activated (as discussed in Jensen and Nugent 2017), and this is a possible explanation for the multiple droplet peaks.

Figure 5a, c indeed shows that the DSD near the end of the simulation has a rightmost peak which is nearly entirely composed of unactivated droplets. At the same time, the central peak

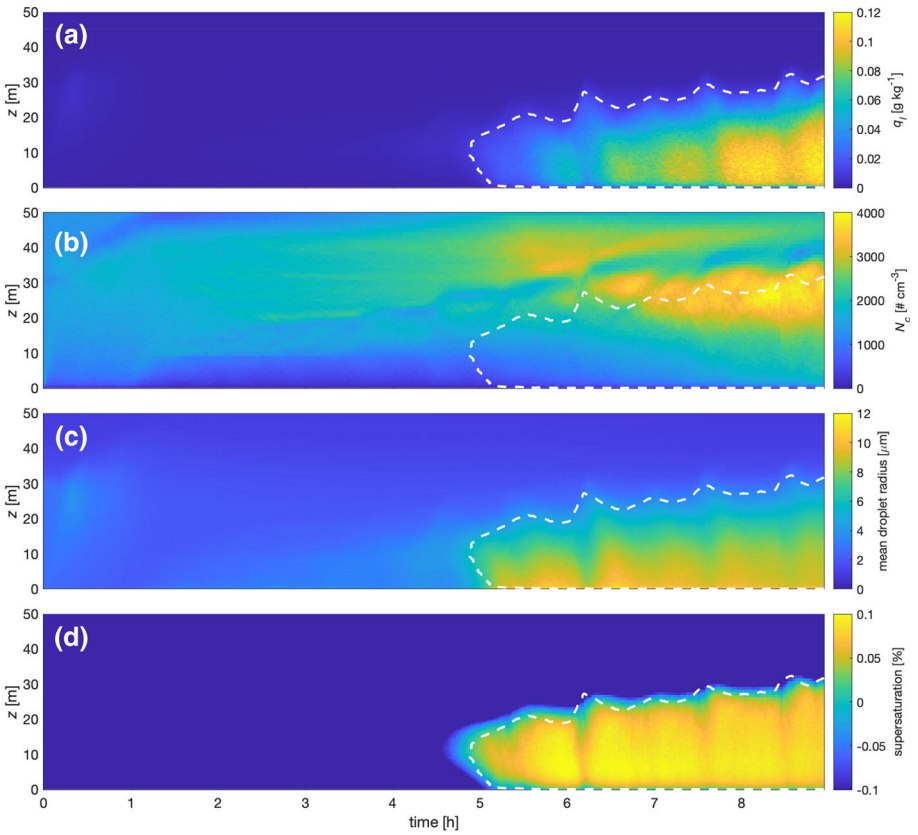


**Fig. 3** Time–height plot of planar–averaged **a** liquid water mixing ratio, **b** total number concentration of aerosols and droplets, **c** mean droplet radius, **d** supersaturation. The white dashed lines indicate the $q_l = 0.01$ g kg$^{-1}$ threshold for fog

is nearly entirely composed of activated droplets, and the leftmost peak is unactivated. Here, the activation state is defined by checking whether the diameter is larger than the critical diameter according to Köhler theory, and the results suggest that the largest droplets in the fog layer, which exceed diameters of $d_p \approx 10$ µm, still remain below their critical diameters even at near-drizzle sizes (see Fig. 1d).

To further investigate this somewhat counterintuitive result, Fig. 5b, d partitions the DSD based on the hygroscopicity $\kappa$; that is, the blue shades correspond to probability density functions accounting only for superdroplets with either $\kappa^i = 0.6$ or $\kappa^i = 1.2$. Doing so reveals an explanation behind the multiple droplet peaks. The rightmost peak, centred around $d_\mathrm{p} \approx 30$ µm, is entirely composed of salt particles with $\kappa = 1.2$, and according to Fig. 5a, c these are also droplets which are technically activated according to their critical diameter. In this particular case, based on the aerosol spectrum measured during C-FOG shown in Fig. 1b, the overall number of these highly hygroscopic, coarse-mode aerosols is insufficient for absorbing all of the excess moisture that accumulates during the fog initiation. Therefore, large particles with $\kappa = 0.6$ begin to activate and grow, resulting in the droplet peak centred at $d_\mathrm{p} \approx 3$ µm. The leftmost peak seen in the numerical DSD at $d_\mathrm{p} \approx 100$ nm (not seen in

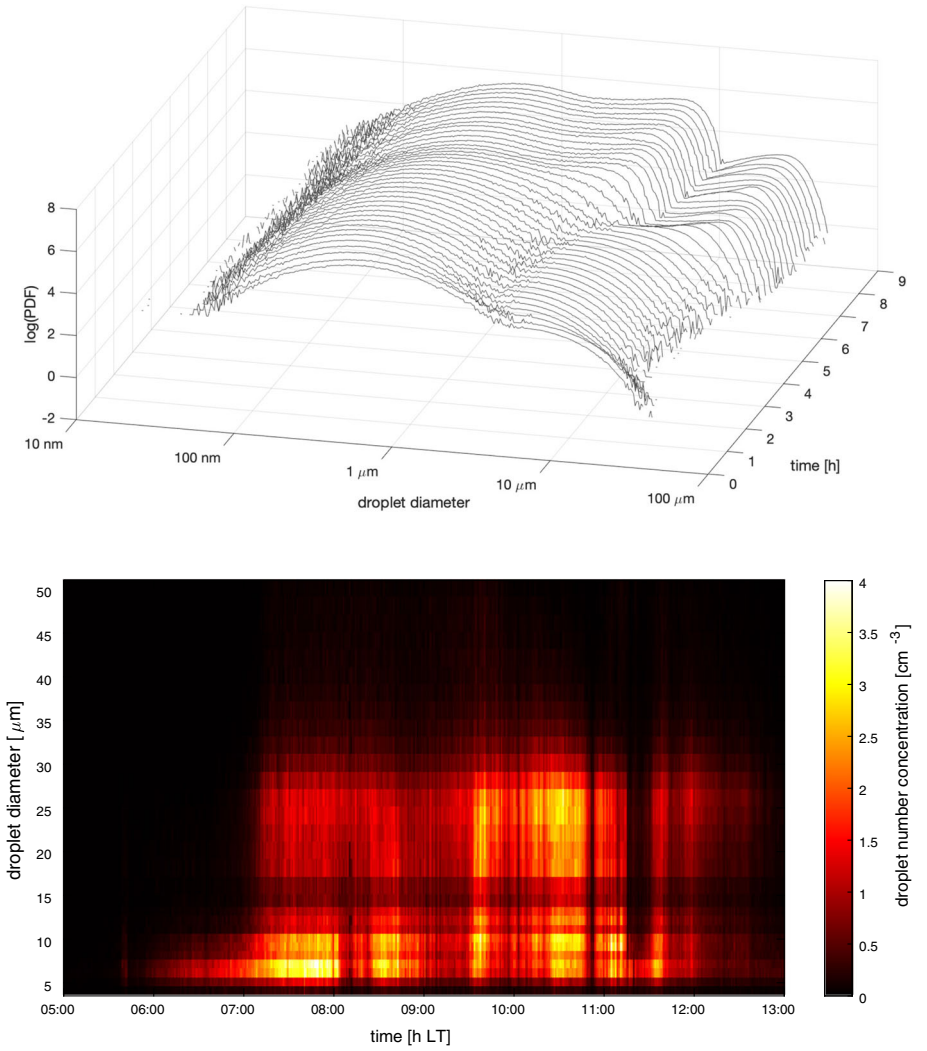


**Fig. 4** Upper: wire plot of the DSD evolution over the course of the simulation. Lower: observed DSD during a marine fog episode off the south-east coast of Nova Scotia during the C-FOG field campaign

Fig. 4b since this is below the minimum FM120 threshold) simply represents the original accumulation mode particles which undergo condensational growth but remain unactivated.

A question then persists as to why the largest, salt-based droplets appear to remain unactivated, despite being more hygroscopic and growing to relatively large diameters. The explanation for this is simply because the time scale for droplet growth (as governed by Eq. 7; see discussions in Andreas 1990 or Veron 2015) can be up to $\mathcal{O}(10\text{ s})$ for droplets of this size. Due to gravitational settling, however, these large coarse-mode droplets rapidly sediment out of the domain, in times closer to $\mathcal{O}(1\text{ s})$. Thus, although these droplets are indeed growing and are behaving as though activated (e.g., they are experiencing supersaturations above their critical value and are taking on liquid water; see Fig. 1c), they do not live long enough to grow to sizes which exceed their relatively large critical diameters (see Fig. 1d). As a result, a classification according to critical diameter exceedance would indicate that

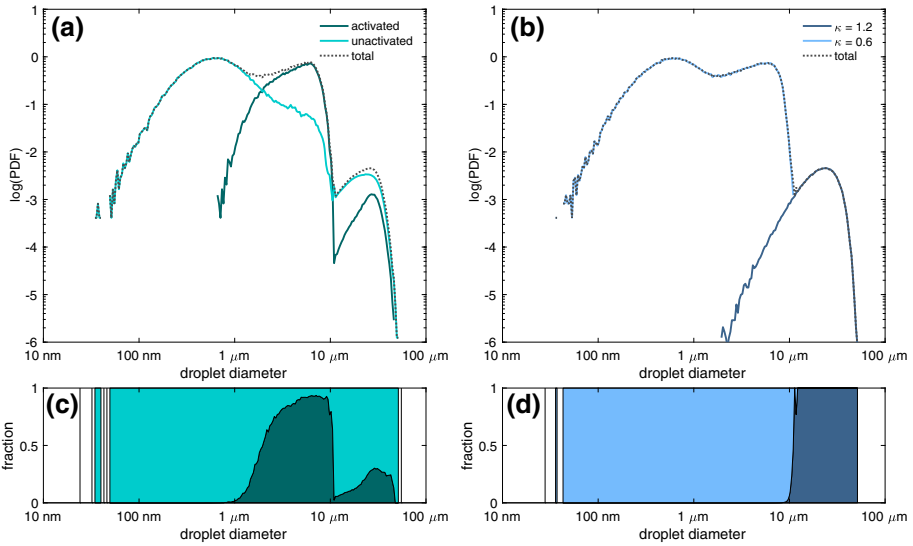


**Fig. 5** The DSD partitioned by **a** droplet activation status and **b** droplet hygroscopicity; **c** and **d** show the fraction of droplets falling into each activation and hygroscopicity category, respectively, at each droplet diameter

these are technically unactivated, because a steady-state theory is being applied to a situation where the droplet growth is slow but transient. Therefore the presence of large, unactivated droplets noted by Jensen and Nugent (2017) certainly seems plausible given the measured dry aerosol spectra in the C-FOG campaign.

It is, therefore, the disparity between the hygroscopicity of the accumulation and coarse-mode aerosols, combined with the limited availability of marine salt particles, which leads to the dual droplet peaks in the numerical and observed data of Fig. 4; we believe that this is the explanation for the qualitative shape in the C-FOG data as well. Furthermore, the droplets in the rightmost peak are sufficiently large that they can be classified as drizzle, and it is important to highlight that these form in the absence of any collision-coalescence mechanism. Condensational growth of hygroscopic marine salt particles is adequate for providing droplets that grow relatively heavy and settle out more rapidly; this has been argued by Jensen and Nugent (2017) among others. We also emphasize that this analysis of constructing the DSD based on aerosol composition would be impossible for both standard bulk and bin microphysical models though extensions have been implemented that can capture this behaviour (Lebo and Seinfeld 2011).

Finally, from the numerical DSD data, it is also instructive to view the progression of the DSD with height at a single point in time—this is shown in Fig. 6. Typically, as in the C-FOG campaign, droplet size measurements are restricted to a single height, particularly in marine settings where logistical challenges are a limiting factor, and questions often remain regarding the uniformity of measured DSDs with height. What Fig. 6 demonstrates, however, is that while perhaps capturing similar qualitative features of the DSD, this single-height strategy is subject to a significant quantitative sensitivity with height. Within the fog layer ($z \lesssim 30$ m), a closer proximity to the sea surface corresponds to relative increase in both rightmost peaks at the expense of the accumulation peak. The increased relative humidity at the surface apparently activates more droplets, which are then distributed over both droplet peaks, resulting in the increased mean droplet size seen in Fig. 3c. Above the fog top, the DSD

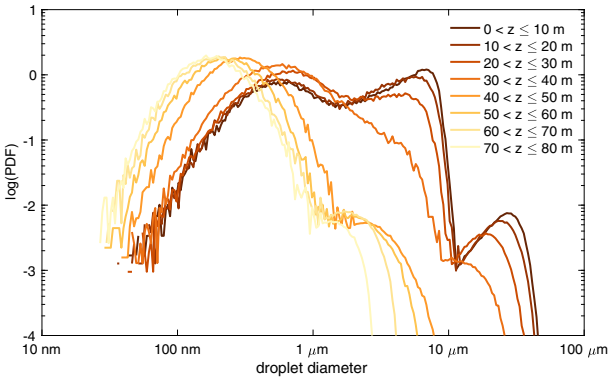


**Fig. 6** Variation of the DSD with height at a single time ($t \approx 8$ h). Each DSD is an average PDF across a 10-m height range, and the fog-top height at this time is at $z \gtrsim 30$ m

continues to change with height, but in a more prescribed way. The shape is governed by the initial profile, and its leftward shift with height simply reflects the decrease of mean relative humidity above the fog. None of the droplets at these heights have been activated. Therefore overall, Fig. 6 demonstrates that qualitative features of the DSD are indeed preserved over the depth of the fog layer, but quantitative details, especially regarding the number of the largest droplets present, can change rapidly. This effect must be considered when interpreting fog DSDs measured at a single height, as also noted by the LCM fog study of Schwenkel and Maronga (2020).

## 4 Conclusions

This work outlines the development of a Lagrangian cloud model, applied to marine fog as observed in the recent C-FOG campaign. This emerging class of microphysical representation offers many advantages over the traditional bulk and bin models, and marine fog is an ideal environment to highlight these benefits and gain physical insight into the physical system. An existing LES model with Lagrangian droplet tracking (the NTLP model; Helgans and Richter 2016; Peng and Richter 2017) was extended following primarily the set-up of Shima et al. (2009). The potential of the LCM for fog studies is demonstrated via simulation of a marine fog episode, with initial conditions based on data recorded during the C-FOG campaign (see Fernando et al. 2020 for details of the field campaign). In particular, the measured aerosol size distribution was used to initialize a large number of superdroplets in the LES domain, and their DSD was tracked in time as the simulated fog developed.

Overall, the fog in the LES–LCM simulation exhibits many of the qualitative features observed during C-FOG, but we focus in particular on the bimodal nature of the fog DSD. By assuming that the accumulation and coarse-mode peaks of the initial aerosol distribution result primarily from continental and marine sources, respectively, and therefore have distinct compositions, the LCM allows for a straightforward dichotomy of hygrosopicity to be prescribed for each. Rather than being caused by collision-coalescence, the two peaks above $d_\mathrm{p} \approx 1$ μm reflect particles of different types. Many of coarse-mode aerosols, which are modelled with a hygroscopicity corresponding to sea salt, technically remain unactivated (as determined by comparing their diameter to the critical diameter) but grow continuously throughout their relatively short lifetime. The relatively low number of these aerosols, how-

ever, causes a large number of the lower hygroscopicity aerosols to activate as well. A larger background concentration of coarse-mode aerosols may therefore preclude the existence of the dual peaks, but this may not be likely at such low wind speeds.

We conclude by stating that the LES–LCM model is a powerful tool which can be used to understand the combined effects of turbulence and microphysical processes. While the primary disadvantages are associated with potential numerical costs of providing a sufficient number of superdroplets, this method will undoubtedly yield insight where traditional models have lacked, particularly in the area of marine fog where much remains unknown.

**Acknowledgements** This research was funded by the Office of Naval Research Award N00014-18-1-2472 entitled Toward Improving Coastal Fog Prediction (C-FOG). Computer resources were made available through the Notre Dame Center for Research Computing and the DoD High Performance Computing Modernization Program.

## References

Alduchov OA, Eskridge RE (1996) Improved Magnus form approximation of saturation vapor pressure. J Appl Meteorol 35(4):601–609. https://doi.org/10.1175/1520-0450(1996)035<0601:IMFAOS>2.0.CO;2

Andreas EL (1990) Time constants for the evolution of sea spray droplets. Tellus B 42B(5):481–497. https://doi.org/10.1034/j.1600-0889.1990.t01-3-00007.x

Andrejczuk M, Reisner JM, Henson B, Dubey MK, Jeffery CA (2008) The potential impacts of pollution on a nondrizzling stratus deck: Does aerosol number matter more than type? J Geophys Res Atmos 113(D19):204. https://doi.org/10.1029/2007JD009445

Árnason G, Brown PS (1971) Growth of cloud droplets by condensation: A problem in computational stability. J Atmos Sci 28:72–77. https://doi.org/10.1175/1520-0469(1971)028<0072:GOCDBC>2.0.CO;2

Boutle I, Price J, Kudzotsa I, Kokkola H, Romakkaniemi S (2018) Aerosol-fog interaction and the transition to well-mixed radiation fog. Atmos Chem Phys 18(11):7827–7840

Chandrakar KK, Cantrell W, Chang K, Ciochetto D, Niedermeier D, Ovchinnikov M, Shaw RA, Yang F (2016) Aerosol indirect effect from turbulence-induced broadening of cloud-droplet size distributions. Proc Natl Acad Sci 113(50):14243–14248. https://doi.org/10.1073/pnas.1612686113

Cooper WA (1989) Effects of variable droplet growth histories on droplet size distributions. Part I Theory J Atmos Sci 46(10):1301–1311. https://doi.org/10.1175/1520-0469(1989)046<1301:eovdgh>2.0.co;2

de Lozar A, Mellado JP (2015) Mixing driven by radiative and evaporative cooling at the stratocumulus top. J Atmos Sci 72:4681–4700. https://doi.org/10.1175/JAS-D-15-0087.1

Deardorff JW (1980) Stratocumulus-capped mixed layers derived from a three-dimensional model. Boundary-Layer Meteorol 18(4):495–527. https://doi.org/10.1007/BF00119502

Fernando HJS, Gultepe I, Dorman C, Pardyjak E, Wang Q, Hoch SW, Richter D, Creegan E, Gaberšek S, Bullock T, Hocut C, Chang R, Alappattu D, Dimitrova R, Flagg D, Grachev A, Krishnamurthy R, Singh DK, Lozovatsky I, Nagare B, Sharma A, Wagh S, Wainwright C, Wroblewski M, Yamaguchi R, Bardoel S, Coppersmith RS, Chisholm N, Gonzalez E, Gunawardena N, Hyde O, Morrison T, Olson A, Perelet A, Perrie W, Wang S, Wauer B (2020) C-FOG: Life of coastal fog. In Press, Bull Am Meteorol Soc

Gerber H (1991) Supersaturation and droplet spectral evolution in fog. J Atmos Sci 48(24):2569–2588. https://doi.org/10.1175/1520-0469(1991)048<2569:SADSEI>2.0.CO;2

Golovin A (1963) The solution of the coagulation equation for cloud droplets in a rising air current. Izv Geophys Ser 5:783–791

Grabowski WW, Abade GC (2017) Broadening of cloud droplet spectra through eddy hopping: Turbulent adiabatic parcel simulations. J Atmos Sci 74:1485–1493. https://doi.org/10.1175/JAS-D-17-0043.1

Grabowski WW, Wang LP (2012) Growth of cloud droplets in a turbulent environment. Annu Rev Fluid Mech 45:293–324. https://doi.org/10.1146/annurev-fluid-011212-140750

Grabowski WW, Morrison H, Shima SI, Abade GC, Dziekan P, Pawlowska H (2019) Modeling of cloud microphysics: Can we do better? Bull Am Meteorol Soc 100(4):655–672. https://doi.org/10.1175/bams-d-18-0005.1

Hall WD (1980) A detailed microphysical model within a two-dimensional dynamic framework: Model description and preliminary results. J Atmos Sci 37:2486–2507. https://doi.org/10.1175/1520-0469(1980)037<2486:ADMMWA>2.0.CO;2

Helgans B, Richter DH (2016) Turbulent latent and sensible heat flux in the presence of evaporative droplets. Int J Multiphase Flow 78:1–11. https://doi.org/10.1016/j.ijmultiphaseflow.2015.09.010
Hoffmann F, Raasch S, Noh Y (2015) Entrainment of aerosols and their activation in a shallow cumulus cloud studied with a coupled LCM-LES approach. Atmos Res 156:43–57. https://doi.org/10.1016/j.atmosres.2014.12.008
Hoffmann F, Noh Y, Raasch S (2017) The route to raindrop formation in a shallow Cumulus cloud simulated by a Lagrangian cloud model. J Atmos Sci 74(7):2125–2142. https://doi.org/10.1175/jas-d-16-0220.1
Jensen JB, Nugent AD (2017) Condensational growth of drops formed on giant sea-salt aerosol particles. J Atmos Sci 74(3):679–697. https://doi.org/10.1175/JAS-D-15-0370.1
Khain AP, Beheng KD, Heymsfield A, Korolev A, Krichak SO, Levin Z, Pinsky M, Phillips V, Prabhakaran T, Teller A, van den Heever SC, Yano JI (2015) Representation of microphysical processes in cloud-resolving models: Spectral (bin) microphysics vs. bulk parameterization. Rev Geophys 53:247–322. https://doi.org/10.1002/2014RG000468
Korolev AV (1994) A study of bimodal droplet size distributions in stratiform clouds. Atmos Res 32(1–4):143–170. https://doi.org/10.1016/0169-8095(94)90057-4
Larson VE, Kotenberg KE, Wood NB (2007) An analytic longwave radiation formula for liquid layer clouds. Mon Weather Rev 135:689–699. https://doi.org/10.1175/MWR3315.1
Lebo ZJ, Seinfeld JH (2011) A continuous spectral aerosol-droplet microphysics model. Atmospheric Chemistry and Physics 11:12,297–12,316, https://doi.org/10.5194/acp-11-12297-2011
Lewis ER, Schwartz SE (2004) Sea salt aerosol production: mechanisms, methods, measurements, and models - a critical review. American Geophysical Union, Washington DC, USA
Maronga B, Bosveld FC (2017) Key parameters for the life cycle of nocturnal radiation fog: a comprehensive large-eddy simulation study. Q J R Meteorol Soc 143:2463–2480. https://doi.org/10.1002/qj.3100
Mazoyer M, Burnet F, Denjean C, Roberts GC, Dupont JC, Elias T (2019) Experimental study of the aerosol impact on fog microphysics at the Instrumented Site for Atmospheric Remote Sensing. Atmos Chem Phys 19:4323–4344. https://doi.org/10.5194/acp-19-4323-2019
Mellado JP (2017) Cloud-top entrainment in stratocumulus clouds. Annu Rev Fluid Mech 49:145–169. https://doi.org/10.1146/annurev-fluid-010816-060231
Mellado JP, Bretherton CS, Stevens B, Wyant MC (2018) DNS and LES for simulating stratocumulus: Better together. J Adv Model Earth Syst 10:1421–1438. https://doi.org/10.1029/2018MS001312
Moeng CH (1984) A large-eddy-simulation model for the study of planetary boundary-layer turbulence. J Atmos Sci 41(13):2052–2062. https://doi.org/10.1175/1520-0469(1984)041<2052:ALESMF>2.0.CO;2
Morrison H, Grabowski WW (2008) Modeling supersaturation and subgrid-scale mixing with two-moment bulk warm microphysics. J Atmos Sci 65:792–812. https://doi.org/10.1175/2007JAS2374.1
Morrison H, Curry JA, Khvorostyanov VI (2005) A new double-moment microphysics parameterization for application in cloud and climate models. Part I: Description. J Atmos Sci 62:1665–1677. https://doi.org/10.1175/JAS3446.1
Morrison H, Witte M, Bryan GH, Harrington JY, Lebo ZJ (2018) Broadening of modeled cloud droplet spectra using bin microphysics in an Eulerian spatial domain. J Atmos Sci 75:4005–4030. https://doi.org/10.1175/jas-d-18-0055.1
Morrison H, van Lier-Walqui M, Fridlind AM, Grabowski WW, Harrington JY, Hoose C, Korolev A, Kumjian MR, Milbrandt JA, Pawlowska H, Posselt DJ, Prat OP, Reimel KJ, Shima SI, Diedenhoven B, Xue L (2020) Confronting the challenge of modeling cloud and precipitation microphysics. J Adv Model Earth Syst. https://doi.org/10.1029/2019ms001689
Nakanishi M (2000) Large-eddy simulation of radiation fog. Boundary-Layer Meteorol 94:461–493. https://doi.org/10.1023/A:1002490423389
Noh Y, Oh D, Hoffmann F, Raasch S (2018) A cloud microphysics parameterization for shallow cumulus clouds based on Lagrangian cloud model simulations. J Atmos Sci 75:4031–4047. https://doi.org/10.1175/JAS-D-18-0080.1
Park H, Sherman T, Freire LS, Wang G, Bolster D, Xian P, Sorooshian A, Reid JS, Richter DH (2020) Predicting vertical concentration profiles in the marine atmospheric boundary layer with a Markov chain random walk model. J Geophys Res Atmos p In Press
Peng T, Richter DH (2017) Influence of evaporating droplets in the turbulent marine atmospheric boundary layer. Boundary-Layer Meteorol 165:1–22. https://doi.org/10.1007/s10546-017-0285-7
Peng T, Richter DH (2019) Sea spray and its feedback effects: Assessing bulk algorithms of air-sea heat fluxes via direct numerical simulations. J Phys Oceanogr 49:1403–1421. https://doi.org/10.1175/JPO-D-18-0193.1

Petters MD, Kreidenweis SM (2007) A single parameter representation of hygroscopic growth and cloud condensation nucleus activity. Atmos Chem Phys 7:1961–1971. https://doi.org/10.5194/acp-7-1961-2007

Pruppacher HR, Klett JD (1997) Microphysics of clouds and precipitation. Reidel, Dordrecht, Netherlands

Riechelmann T, Noh Y, Raasch S (2012) A new method for large-eddy simulations of clouds with Lagrangian droplets including the effects of turbulent collision. New J Phys 14(065):008. https://doi.org/10.1088/1367-2630/14/6/065008

Rogers RR, Yau MK (1996) A short course in cloud physics. Elsevier, Burlington, Massachusetts, USA

Sardina G, Picano F, Brandt L, Caballero R (2015) Continuous growth of droplet size variance due to condensation in turbulent clouds. Phys Rev Lett 115(184):501. https://doi.org/10.1103/PhysRevLett.115.184501

Schwenkel J, Maronga B (2020) Towards a better representation of fog microphysics in large-eddy simulations based on an embedded Lagrangian cloud model. Atmosphere 11:466. https://doi.org/10.3390/ATMOS11050466

Shaw RA (2003) Particle-turbulence interactions in atmospheric clouds. Annu Rev Fluid Mech 35:183–227. https://doi.org/10.1146/annurev.fluid.35.101101.161125

Shen C, Zhao C, Ma N, Tao J, Zhao G, Yu Y, Kuang Y (2018) Method to estimate water vapor supersaturation in the ambient activation process using aerosol and droplet measurement data. J Geophys Res Atmos 123(18):606–10. https://doi.org/10.1029/2018JD028315

Shima S, Kusano K, Kawano A, Sugiyama T, Kawahara S (2009) The super-droplet method for the numerical simulation of clouds and precipitation: A particle-based and probabilistic microphysics model coupled with a non-hydrostatic model. Q J R Meteorol Soc 135:1307–1320. https://doi.org/10.1002/qj.441

Sölch I, Kärcher B (2010) A large-eddy model for cirrus clouds with explicit aerosol and ice microphysics and Lagrangian ice particle tracking. Q J R Meteorol Soc 136:2074–2093. https://doi.org/10.1002/qj.689

Spalart PR, Moser RD, Rogers MM (1991) Spectral methods for the Navier-Stokes equations with one infinite and two periodic directions. J Comput Phys 96:297–324. https://doi.org/10.1016/0021-9991(91)90238-G

Squires P (1952) The growth of cloud drops by condensation I. General considerations. Australian Journal of Scientific Research 5(1):59–86, https://doi.org/10.1071/CH9520059

Sullivan PP, Patton EG (2011) The effect of mesh resolution on convective boundary layer statistics and structures generated by large-eddy simulation. J Atmos Sci 68:2395–2415. https://doi.org/10.1175/JAS-D-10-05010.1

Sullivan PP, McWilliams JC, Moeng CH (1994) A subgrid-scale model for large-eddy simulation of planetary boundary-layer flows. Boundary-Layer Meteorol 71:247–276. https://doi.org/10.1007/BF00713741

Sweet J, Richter DH, Thain D (2018) GPU acceleration of Eulerian-Lagrangian particle-laden turbulent flow simulations. Int J Multiphase Flow 99:437–445. https://doi.org/10.1016/j.ijmultiphaseflow.2017.11.010

Thouron O, Brenguier JL, Burnet F (2012) Supersaturation calculation in large eddy simulation models for prediction of the droplet number concentration. Geosci Model Dev 5(3):761–772. https://doi.org/10.5194/gmd-5-761-2012

Unterstrasser S, Hoffmann F, Lerch M (2017) Collection/aggregation algorithms in Lagrangian cloud microphysical models: Rigorous evaluation in box model simulations. Geosci Model Dev 10:1521–1548. https://doi.org/10.5194/gmd-10-1521-2017

Vaillancourt PA, Yau MK, Grabowski WW (2002) Microscopic approach to cloud droplet growth by condensation. Part I: Model description and results without turbulence. J Atmos Sci 59(24):3421–3435, https://doi.org/10.1175/1520-0469(2002)059<3421:MATCDG>2.0.CO;2

Veron F (2015) Ocean spray. Annu Rev Fluid Mech 47:507–538. https://doi.org/10.1146/annurev-fluid-010814-014651

Wainwright C, Richter DH (2020) Investigating the sensitivity of marine fog to physical and microphysical processes using large-eddy simulation. Under review in Boundary-Layer Meteorol

Weil JC, Sullivan PP, Moeng CH (2004) The use of large-eddy simulations in Lagrangian particle dispersion models. J Atmos Sci 61:2877–2887. https://doi.org/10.1175/JAS-3302.1

Zhang X, Massoli P, Quinn PK, Bates TS, Cappa CD (2014) Hygroscopic growth of submicron and supermicron aerosols in the marine boundary layer. J Geophys Res-Atmos 119:8384–8399. https://doi.org/10.1002/2013JD021213